JOURNAL OF AIRCRAFT
Vol. 36, No. 6, November–December 1999

Anti-Icing System Simulation Using CANICE

François Morency*
École Polytechnique de Montréal, Montréal, Québec, H3C 3A7, Canada
Fatih Tezok†
Bombardier Aerospace, Dorval, Québec, H4S 1Y9, Canada
and
Ion Paraschivoiu‡
École Polytechnique de Montréal, Montréal, Québec, H3C 3A7, Canada

A mathematical model of a hot air anti-icing system and its implementation in the ice accretion simulation code CANICE are presented. The icing code is used to predict the surface temperature and the amount of runback water for given atmospheric conditions and heat flux distribution from an anti-icing device. The external boundary layer is modeled with an integral method. Velocity and temperature distribution in the water film are estimated using a polynomial approximation. Conduction in the airfoil skin is taken into account with a one-dimension model. Numerical results are compared with experimental and numerical results from NASA for three different icing conditions. The comparison shows that surface temperatures are very sensitive to the water droplet impingement limits. The integral method used here failed to predict correctly the heat transfer coefficients in the transition region of the boundary layer. When experimental heat transfer coefficients are used, the model gives satisfactory results.

Nomenclature

A	= control volume surface, m^2
A_c	= cross surface area of the metal skin, m^2
A_T, B_T, C_T	= polynomial coefficients
B	= mass transfer driving force
C_f	= friction coefficient
c_p	= specific heat of air, J/(kg K)
c_w	= specific heat of water, J/(kg K)
$c_{w,g}$	= specific heat of liquid ($T \geq 0$°C) or solid ($T < 0$°C) water
F	= shear force, N/m^2
f	= freezing fraction
g_x	= mass transfer conductance, kg/(m^2 s)
h_{anti}	= internal heat transfer coefficient, W/(m^2 K)
h_x	= heat transfer coefficient, W/(m^2 K)
k	= thermal conductivity, W/(m K)
L_e	= latent heat of evaporation, J
L_f	= latent heat of fusion, J
L_s	= latent heat of sublimation, J
l	= $1/2 Re_\theta C_f$
M	= $m_{\text{in}} + m_{\text{imp}} - m_{\text{vap}}$
m	= mass flow rate, kg/s
$\dot{m}$	= mass flux, kg/(m^2 s)
$m_{\text{H}_2\text{O}}$	= mass concentration of water (mass fraction)
N_{imp}	= number of impacts on a panel
Nu	= Nusselt number, $Pr\,Re\,St$
P	= pressure, N/m^2
$P_{\text{H}_2\text{O}}$	= vapor pressure of water, N/m^2
Pr	= Prandtl number
Q_{anti}	= heat coming from anti-icing system, W/m^2
Q_{loss}	= heat flux leaving the water film, W/m^2
Q_{wall}	= heat flux coming out of the wall, W/m^2
Re	= Reynolds number, $u_e x/\nu$ or $u_e \theta/\nu$
r	= recovery factor, 0.875
St	= Stanton number, $h_x/(\rho u_e C_p)$
s	= wrap distance from the stagnation point, m
T	= temperature, K or °C
T_{anti}	= internal temperature in the anti-icing system, K
T_b	= bulk temperature, K
	$\dfrac{\rho_w \int_0^\delta u_w T_w \, \mathrm{d}y}{m}$
T_{wall}	= wall temperature, K
T_0	= reference temperature, K
U_δ	= water velocity at the interface water–air, m/s
U_∞	= freestream velocity, m/s
u	= velocity, m/s
x, y	= spatial coordinate, m
β	= local collection efficiency
γ	= mass diffusion coefficient, kg/(m s)
Δs	= surface distance between two impact points, m
Δs_p	= panel length, m
Δy	= distance at the start between two trajectories, m
$\delta(x)$	= local water film thickness, m
θ	= momentum thickness, m
λ	= dimensionless pressure gradient
ν	= kinematic viscosity, m^2/s
ρ	= density, kg/m^3
τ	= shear stress exerted by air, N/m^2
[ ]	= characteristic dimension

Subscripts

a	= property of air
e	= evaluated at the edge of the boundary layer
gl	= ice
imp	= relative to the impinging droplet
in	= entering a control volume
out	= leaving a control volume
s	= evaluated at the runback water surface
vap	= vapor

Presented as Paper 98-0192 at the AIAA 36th Aerospace Sciences Meeting, Reno, NV; received 18 January 1999; revision received 23 May 1999; accepted for publication 24 May 1999.

*Ph.D. Student, Département de Génie Mécanique, CP 6079, Succ. Centre Ville. AIAA Student Member.
†Staff Specialist, Advanced Aerodynamics, 400 Côte-Vertu.
‡Professor, Département de Génie Mécanique, CP 6079, Succ. Centre Ville. AIAA Associate Fellow.

w = property of liquid water
x = based on x
θ = based on θ
∞ = freestream condition

Introduction

AIRCRAFT ice accretion prediction codes such as LEWICE[1] or CANICE[2] have now been in use for several years by aircraft manufacturers to predict ice accretion on wing sections. The mathematical model used in each of this codes comes mainly from Messinger,[3] whereas the numerical method comes from MacArthur.[4] Results obtained with these codes compare well with experiments for rime ice accretion. In the case of glaze ice, when the air temperature is warmer and some of the impinging water flows along the airfoil, experimental ice shapes are more difficult to predict.[5] Apart from improving ice shape prediction, the icing codes must also be able to predict ice accretion on high lift devices and have anti-icing or deicing simulation capabilities.

A few works have been done on anti-icing system simulation.[6] Some of these works start with the mathematical modeling of a deicing system and use it to simulate an anti-icing system.[7] These studies concentrate on transient heat transfer calculations inside a multilayered wall. Some of them also try to solve the phase change and shedding problems.[8] These phenomena do not occur when anti-icing systems are used properly. The works that address specifically anti-icing simulation are concentrated either on predicting the amount of power available from the heat source, in general hot air blown inside the leading edge,[9] or on the analysis of the runback water film.[10]

Most of the work done in anti-icing simulation is due to Al-Khalil[10] (see also Ref. 11). In Refs. 10 and 11, it is suggested that the water will either run down as a continuous film flow or will breakup in rivulets when a minimum critical thickness is reached outside the impinging water area. Velocity profiles inside the runback water film and rivulets are determined with a theoretical relation. Temperature distribution in the water and the wall is found by a finite volume code. The heat coming from the anti-icing device is determined using a known heat transfer coefficient between internal hot air and airfoil skin. Interaction either between external air or between impinging water droplets and the runback water is not taken into account.

Few experimental studies are available to validate numerical results. The first experimental investigations of anti-icing systems were made around 1950. These experiments provide empirical and graphical relations useful in the design of anti-icing systems.[12,13] In the last few years, increasing interest in the improvement of ice protection systems has required that NASA build an experimental database using icing wind-tunnel measurements.[14] Surface temperatures together with heat flux distributions have been measured on a NACA 0012 for several different icing conditions.[15]

The objective of the present work is to compare the available experimental results to the numerical results obtained with an anti-icing system model developed in the context of J. A. Bombardier Aeronautical Chair of École Polytechnique. The droplet impact position and the amount of water that may freeze on the leading-edge surface are computed using CANICE. The mathematical modeling and analysis of the heat transfer are concentrated on the energy balance on the external side of the airfoil when a temperature sufficient to evaporate the impinging water is maintained.

The mathematical model is first presented. Then the highlights of the numerical method used to solve the mathematical model are given. Finally, comparisons with other experimental and numerical results are made.

Anti-Icing Model

Four regions must be studied to develop a complete mathematical model for anti-icing performance predictions: 1) the external flow region, 2) the runback water region, 3) the solid region, and 4) the anti-icing hot air region.

These four regions are shown schematically in Fig. 1. The work presented in this paper is concentrated on the second and third regions. In CANICE, as in other ice accretion prediction codes, only two of the four regions are modeled. The external flow region and the runback water region are modeled separately. The temperature of the solid region is the same as the runback water temperature.

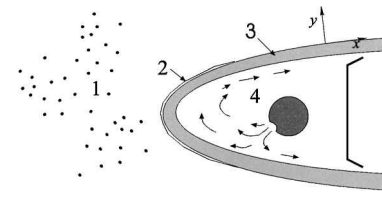

Fig. 1 Different regions in the model of an anti-icing system.

The icing code CANICE is modified to include the temperature gradient in the runback water, to determine the heat transfer in the wall, and to include a simple model of the anti-icing hot air region. An iterative procedure is used to solve the surface temperature distribution and the mass of water evaporated. The two-dimensional models used for each of the four regions are presented in the following subsections.

External Flow Region

The external flow region includes airflow around the airfoil and water droplet trajectories. To begin, a potential solution for the flow around airfoil is found. Starting in the unperturbed region of the flow, we then determine the water droplet trajectories using the potential flow velocity field. From the droplet impingement distribution, the local catch efficiencies are calculated and, thus, the impinging water rate on the airfoil is determined. The procedure used has been described in detail by Brahimi et al.[16]

The friction coefficient, the heat transfer coefficient, and the evaporation rate above the runback water are calculated by solving the boundary layer equations with an integral method.[17] The integral method estimates the friction coefficient C_f and the Stanton number St for laminar and turbulent flows.

For the laminar boundary layer, the momentum thickness θ is first evaluated with the help of tangential velocity at the wall u_e found from the potential flow solution,[18]

$$\theta = \left(\frac{0.45 \nu_a}{u_e^6} \int_0^x u_e^5 \right)^{0.5} \tag{1}$$

The friction coefficient C_f can then be found with the following relations[19]:

$$\lambda = \frac{\theta^2}{\nu_a} \frac{\mathrm{d}u_e}{\mathrm{d}x} \tag{2}$$

$$l(\lambda) = 0.22 + 1.57\lambda - 1.8\lambda^2 \qquad 0 < \lambda < 0.1$$

$$l(\lambda) = 0.22 + 1.402\lambda - \frac{0.018\lambda}{\lambda + 0.107} \qquad -0.1 < \lambda < 0 \tag{3}$$

and, finally,

$$C_f = 2[l(\lambda)/Re_\theta] \tag{4}$$

A relation for the local Stanton number St is suggested by Kays and Crawford[18] for flow over a constant temperature body of arbitrary shape,

$$St = 0.418 \frac{\nu_a^{0.5} (\rho_a u_e)^{0.435}}{\left[\int_0^x (\rho_a u_e)^{1.87} \, \mathrm{d}x \right]^{0.5}} \tag{5}$$

With the definition of the Stanton number, the local heat transfer coefficient h_x is determined.

The transition point location is either imposed or calculated using the following relation[19]:

$$Re_\theta > 1.174[1 + (22{,}400/Re_x)] Re_x^{0.46} \tag{6}$$

For the turbulent boundary layer, the friction coefficient and the Stanton number are estimated from relations for turbulent flow over a smooth surface,[18]

$$\theta = \frac{0.036\nu_a^{0.2}}{u_e^{3.29}}\left(\int_0^x u_e^{3.86}\,\mathrm{d}x\right)^{0.8} \tag{7}$$

$$C_f/2 = 0.0125 Re_\theta^{-\frac{1}{4}} \tag{8}$$

$$St = 0.0287 Pr^{-0.4}\frac{(T_s - T_e)^{0.25}\nu_a^{0.2}}{\left[\int_0^x (T_s - T_e)^{1.25}\rho_a u_e\,\mathrm{d}x\right]^{0.2}} \tag{9}$$

The evaporation rate $\dot{m}_{\text{vap}}$ is given by the product of the conductance g_x and the mass transfer driving force B (Ref. 18),

$$\dot{m}_{\text{vap}} = g_x B \tag{10}$$

The driving force B is function of the mass concentration of water at the edge of the boundary layer, $m_{\text{H}_2\text{O},e}$, and the mass concentration of water on the runback water surface, $m_{\text{H}_2\text{O},s}$,

$$B = \frac{m_{\text{H}_2\text{O},e} - m_{\text{H}_2\text{O},s}}{m_{\text{H}_2\text{O},s} - 1} \tag{11}$$

The mass concentration of water is related to the water vapor pressure $P_{\text{H}_2\text{O}}$ at the local temperature,

$$m_{\text{H}_2\text{O}} = P_{\text{H}_2\text{O}}\Big/\left(1.61P_e - 0.61P_{\text{H}_2\text{O}}\right) \tag{12}$$

The vapor pressure is a function of the temperature and is given by a polynomial interpolation from the American Society of Mechanical Engineers steam table.[20]

For temperature near 0°C, Eq. (11) becomes

$$B = \frac{P_{\text{H}_2\text{O},s} - P_{\text{H}_2\text{O},e}}{1.61P_e} \tag{13}$$

which is the formulation used in icing codes.

The conductance, for a boundary layer with B near 0, is related to the local heat transfer coefficient h_x,

$$g_x = (h_x/c_p)\left[Pr^a\Big/(\nu_a/\gamma)\right] \tag{14}$$

For a laminar boundary layer $a = 0.6$, and for a turbulent boundary layer $a = 0.4$.

Runback Water Region

Water coming from the droplets that hit the airfoil will freeze, runback, or evaporate. The runback water is modeled as a continuous film flow on the airfoil surface. For a thin film whose thickness $\delta(x)$ changes slowly, inertia terms in the Navier–Stokes equations are negligible. The momentum equation in the x direction becomes a simple balance between the pressure gradient and the viscous forces (see Fig. 2),

$$\frac{1}{\rho_w}\frac{\mathrm{d}P}{\mathrm{d}x} = \nu_w\frac{\partial^2 u_w}{\partial y^2} \tag{15}$$

The potential flow solution of the external air region gives the value for the pressure gradient. The film flow is driven by the shear force F. For slow water speed compared to airflow, the boundary-layer solution is approximately the same as the one over a stationary wall. Thus, the shear force F is the sum of the wall friction τ found with the boundary-layer integral solution and of the momentum per unit area from incoming water droplet $\dot{m}_{\text{imp}}u_{\text{imp}}$,

$$F = \tau + \dot{m}_{\text{imp}}u_{\text{imp}} \tag{16}$$

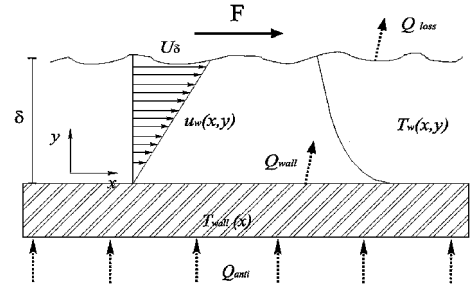

Fig. 2 Water film model.

By the consideration of the no-slip condition at the wall, Eq. (15) can be solved to give a parabolic velocity distribution at every x position,

$$u_w(x, y) = \frac{1}{2\mu_w}\frac{\mathrm{d}P}{\mathrm{d}x}y^2 + \frac{1}{\mu_w}\left[F - \delta(x)\frac{\mathrm{d}p}{\mathrm{d}x}\right]y \tag{17}$$

If the energy rate entering the water film changes slowly, compared to the film thickness δ, the energy equation for the flow described by Eq. (15) becomes

$$\rho_w u_w c_w\frac{\mathrm{d}T_w}{\mathrm{d}x} = \frac{\partial}{\partial y}\left(k_w\frac{\partial T}{\partial y}\right) \tag{18}$$

A parabolic temperature distribution is obtained by integrating Eq. (18) in the y direction,

$$T_w(x, y) = A_T(x)y^2 + B_T(x)y + C_T(x) \tag{19}$$

The heat flux coming from the wall, Q_{wall}, and the heat flux lost to the external airflow, Q_{loss}, respectively, give the temperature slope at the wall and at the air–water interface. With the help of these quantities, values for the polynomial coefficients A_T and B_T are found. The heat flux lost to the airflow includes convection, evaporation, and the energy lost to the impinging droplets,

$$Q_{\text{loss}} = h_x(T_s - T_e - ru_e/c_p) + \dot{m}_{\text{vap}}[c_w(T_s - T_0) + Le] - \dot{m}_{\text{imp}}\left[c_w(T_\infty - T_0) + 0.5u_{\text{imp}}^2\right] \tag{20}$$

For a mass flow rate m, the bulk temperature T_b inside the water film sets the $C_T(x)$ value.

The validity of the approximations made to obtain Eqs. (17) and (19) are discussed in "Validity of the Surface Model" section.

Solid Region

For a thin plate made of material with a uniform conductivity k and a cross surface area A_c, the temperature variation across the thickness can be neglected. Thus, only conduction in direction of the length is considered for the airfoil wall. The airfoil wall essentially redistributes the heat coming from the anti-icing system, Q_{anti},

$$Q_{\text{wall}} = Q_{\text{anti}} + kA_c\frac{\mathrm{d}T_{\text{wall}}}{\mathrm{d}x^2} \tag{21}$$

Anti-Icing Hot Air Region

The anti-icing hot air region is modeled with a local internal convection coefficient h_{anti} or an imposed heat flux Q_{anti}. The local convection coefficient is considered to be known from previous calculations or experiments. When the heat transfer coefficient is specified, heat flux coming from the anti-icing system is evaluated with the help of the internal airflow temperature T_{anti} and the local wall temperature T_{wall},

$$Q_{\text{anti}} = h_{\text{anti}}(T_{\text{anti}} - T_{\text{wall}}) \tag{22}$$

Numerical Method

The model of the external flow region is based on the usual icing code formulation.[1,2] The potential flow around the airfoil is solved by using the panel method of Hess and Smith (see Ref. 19). Each individual droplet trajectory, starting at an unperturbed point upstream of the airfoil, is calculated with a variable time step Runge–Kutta method of order five (Ref. 21).

Once the first two impact points have been found, the local collection efficiency β is found from the ratio of the distance Δy at the start of trajectories calculation to the surface distance between impact Δs,

$$\beta = \frac{\Delta y}{\Delta s} \tag{23}$$

With the help of this collection efficiency, the next step Δy between starting points of trajectories is fixed by the number of impacts N_{imp} on a panel,

$$\Delta y = \beta \Delta s_p N_{\text{imp}} \tag{24}$$

The rate of impinging water on each panel of the discretized profile is then calculated using the collection efficiency.[16]

The heat transfer coefficient and the friction coefficient on the runback water surface are evaluated at each panel center using an integral method to solve the boundary layer.[17] At the stagnation point, the starting value for the momentum thickness θ (Ref. 19) and the Nusselt number Nu (Ref. 18) are given, respectively, by

$$\theta = \sqrt{\frac{0.075 \nu_a}{\mathrm{d}u_e/\mathrm{d}s}} \tag{25}$$

$$Nu = 0.496 \sqrt{u_e x / \nu_a} \tag{26}$$

The evaporation rate is calculated using Eq. (14) for the conductance and the vapor pressure at the water film surface.

The surface of the airfoil is divided into control volumes of the length of the panel, as in the work of MacArthur.[4] A mass and an energy balance of each control volume is used to obtain the airfoil surface temperature.

The mass balance equation can be written as

$$m_{\text{in}} + m_{\text{imp}} = m_{\text{gl}} + m_{\text{vap}} + m_{\text{out}} \tag{27}$$

A freezing fraction f is defined so that it ranges from 0 (no ice) to 1 (no runback water, $m_{\text{out}} = 0$),

$$f = m_{\text{gl}} / (m_{\text{in}} + m_{\text{imp}} - m_{\text{vap}}) \tag{28}$$

The mass of water running back can then be expressed as a function of the impinging water rate m_{imp}, the incoming water rate m_{in}, and the evaporation rate m_{vap},

$$m_{\text{out}} = (1 - f)(m_{\text{in}} + m_{\text{imp}} - m_{\text{vap}}) \tag{29}$$

After some simplifications, a single energy balance equation is obtained for the three possible surface cases: 1) dry ($f = 1$), 2) wet ($0 < f < 1$), and 3) liquid ($f = 0$),

$$\begin{aligned} f M (c_w T_s - L_f) + m_{\text{vap}} (c_{w,g} T_s - L_f) + m_{\text{vap}} L_s + (1 - f) M c_w T_s \\ = m_{\text{imp}} \left(c_w T_\infty + U_\infty^2 / 2 \right) + h_x A \left[\left(r u_e^2 / 2 c_p \right) - (T_s - T_\infty) \right] \\ + Q_{\text{wall}} + m_{\text{in}} c_w T_b \end{aligned} \tag{30}$$

The airfoil wall is divided into control volumes of panel length and of thickness of the airfoil wall to solve Eq. (21). The surface temperature and the amount of water that evaporates for a given internal heat transfer coefficient are found with an iterative procedure. An initial wall temperature distribution is used to obtain the heat flux Q_{anti} from the anti-icing system. Then, the heat flux coming out from the airfoil wall Q_{wall} is calculated. This heat flux is used to find a new wall temperature T_{wall}. The heat flux Q_{anti}, from the anti-icing hot air region corresponding to this surface temperature, is then evaluated again and used to calculate a new wall temperature. The iterative process stops when energy entering the airfoil wall equals energy leaving the airfoil wall. Relaxation is needed for convergence of the iterative process.

Results and Discussion

CANICE is used to compute ice catch rates and ice shapes over Canadair supercritical airfoils. It has already been validated against experimental data collected during tests conducted at the NASA John H. Glen Research Center at Lewis Field Icing Tunnel Test Facility (see Ref. 22).

First, a comparison between the proposed runback water model and the one of Al-Khalil[10] is presented. Then, surface temperature predictions obtained with the model are compared with experimental and numerical results of Al-Khalil et al.[15] for a NACA 0012 airfoil. Finally, validity of the hypothesis made in the development of the mathematical model is verified.

Runback Water Results

Results obtained with the runback water model are compared to those of Al-Khalil[10] for a theoretical case described in detail. A flat plate case is suggested for which the impinging rate as well as the inside and the outside convection coefficients are presented in Fig. 3. The flat plate is made of aluminum and has a thermal conductivity $k = 100$ W/m K. The inside air temperature changes linearly from 220 to 120°C. The temperature and pressure outside the boundary layer are, respectively, −10°C and 0.5 atm. The shear force that drives the water film is 10 Pa.

The Al-Khalil model[10] is based on the assumption that velocity changes linearly in the continuous film flow. The temperature variation across runback water and in the wall is found with a two-dimensional finite volume method. Although this model simulates the breakup of the water film into rivulets, results for a continuous film flow are also available in this flat plate case.

In Fig. 4, the temperature distributions along the flat plate obtained with the two models are shown. The temperatures compare well, except at the end of the flat plate. This deviation probably comes from differences in the thermal boundary conditions. Al-Khalil's model[10] seems to consider only the latent evaporation heat, neglecting the vapor energy leaving the water film.

The water film thickness is also shown in Fig. 5. When a constant water viscosity is used, the two models show practically the same results. When the water viscosity is allowed to change with the temperature in the model, the results are quite different. The use of a constant or variable viscosity μ_w has practically no impact on the average temperature results because the water film is so thin that the temperature variation across the thickness is negligible.

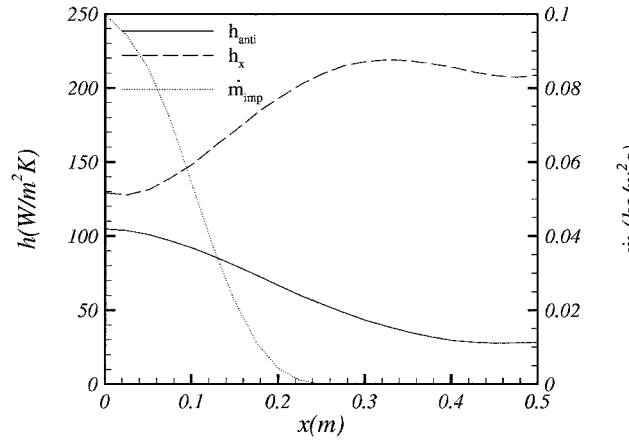

Fig. 3 Flat plate case: rate of impinging water, internal and external heat transfer coefficients.

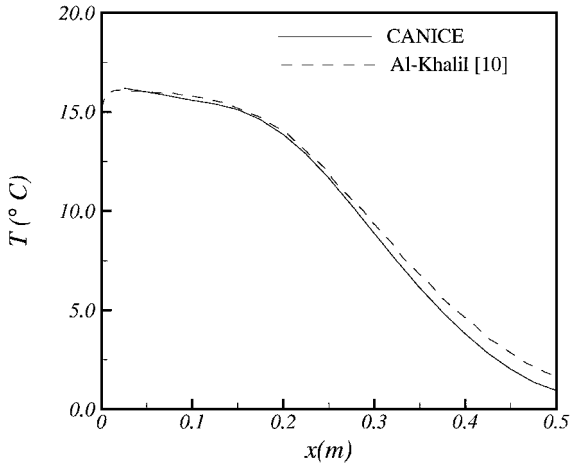

Fig. 4 Average water temperature in the water film.

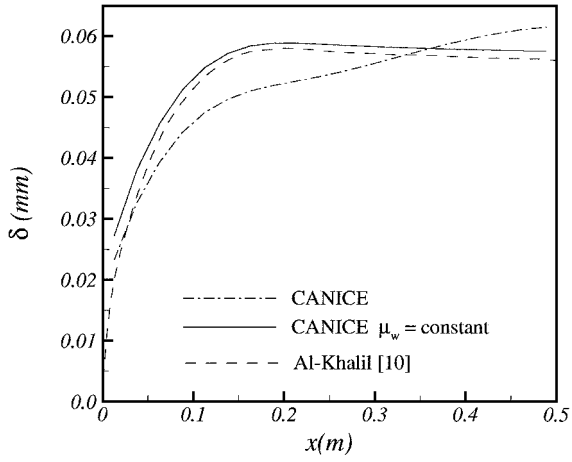

Fig. 5 Water film thickness.

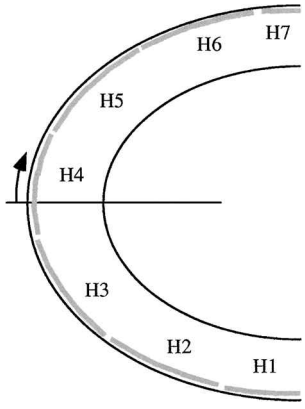

Fig. 6 Heater bands inside the airfoil.

Table 1 Wrap position of the heaters

Heater	Start, cm	End, cm
H1	−9.3599	−5.5499
H2	−5.5499	−3.0099
H3	−3.0099	−0.4699
H4	−0.4699	1.4351
H5	1.4351	3.9751
H6	3.9751	6.5151
H7	6.5151	10.3251

Table 2 Material conductivity and thickness from top to bottom of the ice protection system

Layer	Conductivity, W/(m K)	Thickness, cm
1	16.27	0.02
2	0.256	0.028
3	41.02	0.00127
4	0.256	0.028
5	0.294	0.089
6	0.12	0.343

Table 3 Icing conditions for the three selected cases

Icing condition	T_∞, °C	U_∞, m/s	LWC, g/m^3
22A	−7.6	44.7	0.78
35A	−18.8	44.7	0.78
67A	−21.76	89.4	0.55

Table 4 Power from each heater

Icing condition	Heater power densities, kW/m^2						
	H1	H2	H3	H4	H5	H6	H7
22A	9.920	10.230	32.550	46.500	18.600	6.975	10.230
35A	12.090	11.780	34.100	46.500	23.250	6.665	12.710
67A	20.150	21.700	32.550	43.400	26.350	18.600	18.600

Comparison with Experiments

Experiments

Numerical results are compared with the experimental surface temperature distribution obtained by Al-Khalil et al.[15] In their study, a NACA 0012 airfoil, 1.8288-m (6-ft) span and 0.9144 m (36 in) chord, is fitted with an electrothermal ice protection system at the leading edge. The ice protection system consisted of seven heater bands, three on each side of the airfoil and one centered on the leading edge, as shown in Fig. 6. The heater layup was accidentally shifted toward the upper part of the airfoil. Table 1 lists the wrap coordinates of each of the heaters.

The electrothermal ice protection system has six layers of different conductivity and thickness, as Table 2 shows. The third layer is the heating element. Because the present model can only simulate a single layered solid region, an equivalent thermal conductivity is calculated.

With the hypothesis of a constant temperature across thickness, equivalent conductivity can be determined for chordwise conduction. For an equivalent thickness $A_c = 0.500$ cm, the equivalent conductivity is 0.9182 W/(m K) for the system.

In the icing tunnel, 15 icing conditions were tested. The three cases presented here, at 0-deg angle of attack and with a mean volumetric diameter of 20 μm, are described in Table 3. The heater power densities used are presented in Table 4. For these three cases all of the impinging water evaporated in the leading-edge area.

Al-Khalil et al.[15] also give the experimental heat transfer coefficients over a clean airfoil. The numerical calculations of Al-Khalil et al. are done with the experimental heat transfer coefficients.

Collection Efficiencies

Determination of the collection efficiencies and impingement limits are critical in the simulation of an anti-icing system. As will be seen later, temperatures along the airfoil skin depend strongly on the presence of water.

Figure 7 shows the numerical collection efficiencies obtained with CANICE when $U_\infty = 44.7$ m/s. These collection efficiencies are compared with the collection efficiencies used by Al-Khalil et al.[15] The impinging water area is quite larger in the case of Al-Khalil et al., results going from −5 to 5 cm instead of −2.5 to 2.5 cm. Figure 7 also shows the collection efficiencies if we consider that droplets have a Median Volumetric Diameter (MVD) = 20 μm ± 12% and follow a log-normal distribution in the wind tunnel. The impinging area extends a little more because of the large droplets. Nevertheless, CANICE numerical results do not show the slow changing collection efficiencies region of Al-Khalil et al. curves below $\beta = 0.1$.

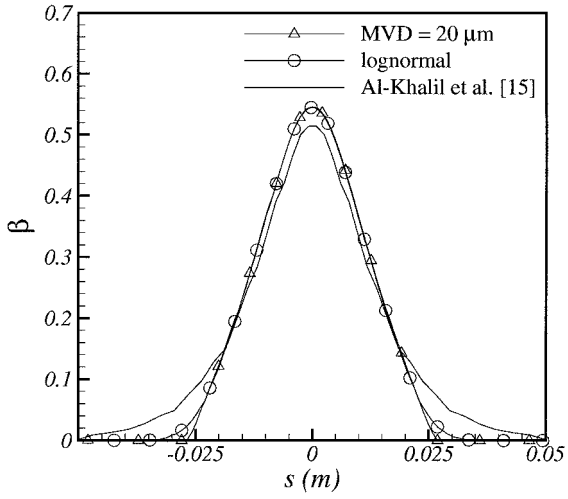

Fig. 7 Collection efficiencies for cases 22A and 35A.

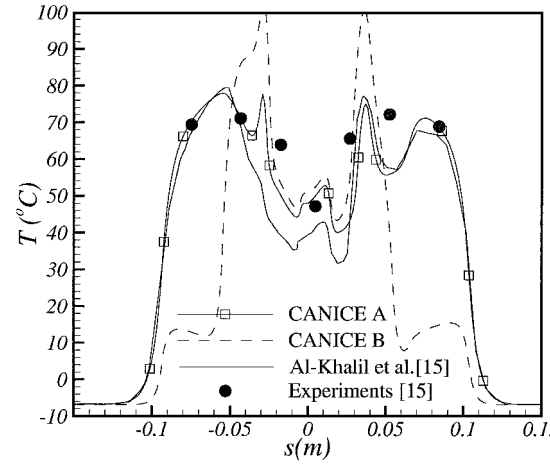

Fig. 9 Comparison of surface temperature distributions for case 22A.

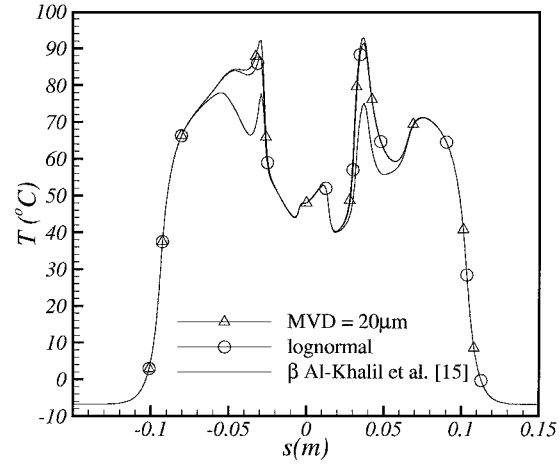

Fig. 8 Surface temperature distribution with three different collection efficiencies distribution for case 22A.

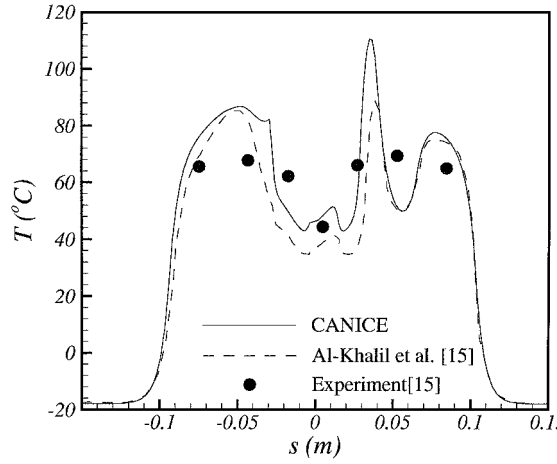

Fig. 10 Comparison of surface temperature distributions for case 35A.

Note that a large number of panels, at least 600 with a sinusoidal distribution, are needed to obtain collection efficiency coefficients in the region below $\beta = 0.05$.

Surface Temperature Distribution

Figure 8 shows the effect of collection efficiency distribution on surface temperature for case 22A of Ref 15. The experimental heat transfer coefficients of Al-Khalil et al.[15] are used for this comparison. When the collection efficiencies distribution of Al-Khalil et al. are used, the maximum temperature near -3 and 3 cm is approximately 10°C. This is because no water runs back after -3 and 3 cm when the CANICE collection efficiencies are used. With a larger impingement region, a part of the heating power is used to evaporate the water between -3 and -5 cm or between 3 and 5 cm. Because of the high water latent heat of evaporation, a small mass of water is sufficient to induce a large fall in the surface temperature.

In Figure 9, numerical surface temperature distributions obtained using Al-Khalil et al.[15] collection efficiencies are presented. In Fig. 9, experimental and numerical results of Al-Khalil et al. are also shown. The curve CANICE A is obtained using the experimental heat transfer coefficient, whereas the curve CANICE B is obtained using the numerical heat transfer coefficient from the integral boundary-layer method.

When the experimental heat transfer coefficients are used, CANICE results, plotted as curve CANICE A, are close to the experimental results. There is a significant difference between the experimental and numerical surface temperature near the 5-cm area. For almost all of the 15 icing cases presented by Al-Khalil et al.,[15] CANICE surface temperature in this area are below the experiment, and it is suspected that this maybe due to an underestimation of the heater power densities.

CANICE A and B curves are similar only between $s = -2$ and 2 cm, when water is still present on the airfoil. When there is no water on the metal skin, surface temperature depends strongly on heat transfer coefficient. In the laminar region of the boundary layer, the heat transfer coefficients from the integral method are below the experimental ones and, thus, surface temperatures are higher for the CANICE B curve. Because the transition region between the laminar and turbulent boundary layers is not modeled by the integral method, the heat transfer coefficients rise abruptly after the transition point is set in $s = \pm 5$ cm. This transition point is set based on experimental observation. The numerical heat transfer coefficients become higher than the experimental ones, and surface temperature falls quickly for CANICE B curve.

CANICE temperature predictions in the leading-edge area are higher than those of Al-Khalil et al.[15] because the driving force B is estimated using Eq. (11) instead of Eq. (13). The evaporation rates in CANICE are, thus, lower.

Results for case 35A of Ref. 15, using experimental heat transfer coefficients and numerical collection efficiency distribution, are shown in Fig. 10. As in case 22A, CANICE surface temperatures are higher than those of Al-Khalil et al.[15] because evaporation rates are lower. When no runback water is present, past -3 and 3 cm, surface temperatures get closer to those of Al-Khalil et al. Because of the smaller impinging area of CANICE, a maximum surface temperature above 100°C occurs.

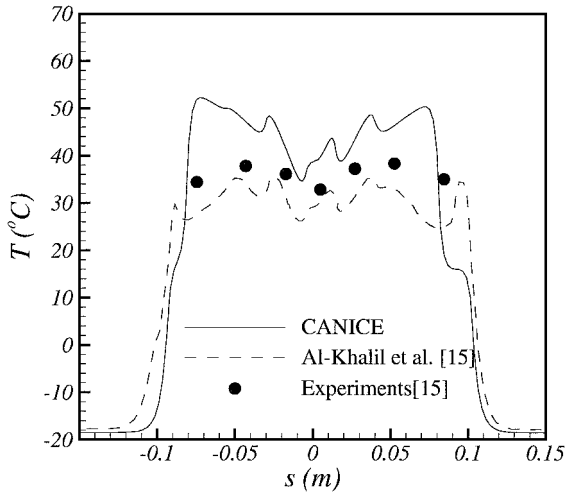

Fig. 11 Comparison of surface temperature distributions for case 67A.

Case 67A of Ref. 15 is presented in Fig. 11. For this case, CANICE collection efficiencies and heat transfer coefficients are used, with an imposed transition near −8 and 8 cm. In this case, there is water rundown until −9 and 9 cm, and surface temperatures are less sensitive to heat transfer coefficient values. Because of this, CANICE results are close to the experimental values, although a significant drop in surface temperature is visible near the transition point, just after a maximum in surface temperature is reached. Again, a proper model of the transition region is needed to induce a gradual change in surface temperature as in the experimental results.

Validity of the Surface Model

The first assumption made in the development of the runback water mathematical model, apart from the assumption of two dimensionality, is that the film flow is continuous. The two others main hypotheses are that droplet impacts do not perturb the water film and that waves do not occur. These three hypotheses, although not a good representation, lead to great simplification of the problem and are almost unavoidable if the problem is to be solved as a stationary one.

Once these assumptions are accepted, two hypotheses lead to the simplified equations used for the runback water model. First, inertia terms in the Navier–Stokes equation can be negligible. This is the case if[23]

$$[\delta]^2/[x]_2 \ll \nu_w/[u][x] \tag{31}$$

The rate of change $[\alpha]$ of thickness in the x direction gives the characteristic length $[x]$,

$$[x] = [\delta]/[\alpha] \tag{32}$$

Typical values for characteristic length are $[u] = 0.02$ m/s, $[\delta] = 3 \times 10^{-6}$ m, $[\alpha] = 0.001$, and $\nu_w = 80 \times 10^{-8}$ m^2/s. With these values, Eq. (31) is justified.

The second hypothesis is that a fully developed temperature profile exists. This is true for[18]

$$[x]/[\delta] > 0.1([u]/[\delta])\nu_w Pr_w \tag{33}$$

The extent of a heating area is taken as the characteristic length $[x]$. With $[x] = 0.02$ m and $Pr_w = 7$, Eq. (33) is also justified.

Temperature variations across the electrothermal anti-icing device have been measured for case 22A in the leading-edge area.[14] A variation of around 6°C occurs between the inner layer and the surface. The difference of temperatures between the heater and the surface is on the order of 0.5°C.

The hypothesis of constant temperature across the metal skin is not accurate if we consider all of the layers in the anti-icing device. Apart from the slight overestimation of the surface temperature, the hypothesis of constant temperature does not model two-dimensional effects well. The two-dimensional effects are present particularly in the border of each heater area, as well as at the end of the runback water area. From the presented results, it is near the end of the runback water area, when energy is transferred from a dry region to a wet region, that two-dimensional effects are the most important.

Conclusions

A mathematical model has been developed to analyze the heat transfer over an airfoil in icing conditions with hot air anti-icing systems. A simple runback water temperature model has been suggested. This simple model gives good results when compared to numerical results of Al-Khalil et al.[15] For all of the cases studied here, the runback water film is so thin that temperatures change linearly across the water film. The main advantage of the present model is the possibility of implementing it in the CANICE code. Hence, ice accretion when not enough heat is provided by the anti-icing system can be simulated.

Numerical results have been compared to experimental results available for a NACA 0012 airfoil with an electrothermal anti-icing device. These comparisons show the sensitivity of the surface temperature to the estimation of the impingement limits and to the mass of water captured. Surface temperatures also highly depend on the local heat transfer coefficient used. A proper model of the heat transfer in the transition region is needed. With the integral method presented here, heat transfer coefficients rise too quickly after the transition point, causing a sharp decrease of the temperature. Unfortunately, experimental measurement points of temperature are too widely spaced to permit a good comparison with the numerical results.

The hypotheses used in the development of the present model appear to be valid for the runback water region. The one-dimensional model of the solid region gives good results, although experimental data showed that the temperature is not constant across the thickness. A temperature profile comparison between the CANICE and Al-Khalil et al.[15] numerical results indicates that the present wall model gives satisfactory results.

Acknowledgments

The authors would like to acknowledge the support of the National Sciences and Engineering Research Council through a cooperative research and development grant with Bombardier Aerospace. The first author would also like to thank the Fonds pour la Formation de Chercheurs et de l'Aide à la Recherche for his scholarship.

References

[1]Ruff, G. A., and Berkowitz, B. M., "Users Manual for the NASA Lewis Ice Accretion Prediction Code (LEWICE)," NASA CR-185 129, May 1990.

[2]Brahimi, M. T., Tran, P., and Paraschivoiu, I., "Numerical Simulation and Thermodynamic Analysis of Ice Accretion on Aircraft Wings," École Polytechnique de Montréal, Project C.D.T C159, Montréal, QC, Canada, May 1994.

[3]Messinger, B. L., "Equilibrium Temperature of an Unheated Icing Surface as a Function of Air Speed," *Journal of the Aeronautical Sciences*, Vol. 20, No. 1, 1953, pp. 29–42.

[4]MacArthur, C. D., "Numerical Simulation of Airfoil Ice Accretion," AIAA Paper 83-0112, Jan. 1983.

[5]Tran, P., Brahimi, M., Paraschivoiu, I., Pueyo, A., and Tezok, F., "Ice Accretion on Aircraft Wings with Thermodynamic Effect," *Journal of Aircraft*, Vol. 32, No. 2, 1994, pp. 444–446.

[6]Thomas, S. K., Cassoni, R. P., and MacArthur, C. D., "Aircraft Anti-Icing and Deicing Techniques and Modeling," *Journal of Aircraft*, Vol. 33, No. 5, 1996, pp. 841–854.

[7]Henry, R., "Development of an Electrothermal De-Icing/Anti-Icing Model," AIAA Paper 92-0526, Jan. 1992.

[8]Wright, W. B., De Witt, K. J., and Keith, T. G., Jr., "Numerical Simulation of Icing, Deicing, and Shedding," AIAA Paper 91-0655, Jan. 1991.

[9]Croce, G., Habashi, W. G., Guèvremont, G., and Tezok, F., "3D Thermal Analysis of an Anti-Icing Device Using FENSAP-ICE," AIAA Paper 98-0198, Jan. 1998.

[10]Al-Khalil, K. M., "Numerical Simulation of an Aircraft Anti-Icing System Incorporating a Rivulet Model for the Runback Water," Ph.D. Dissertation, Univ. of Toledo, Toledo, OH, June 1991.

[11]Al-Khalil, K. M., Keith, T. G., Jr., and De Witt, K. J., "New Concept in Runback Water Modeling for Anti-Iced Aircraft Surfaces," *Journal of Aircraft*, Vol. 30, No. 1, 1993, pp. 41–49.

[12]Gelder, T. F., and Lewis, J. P., "Comparison of Heat Transfer from Airfoil in Natural and Simulated Icing Conditions," NACA TN 2480, Sept. 1951.

[13]Brun, E. A., "Icing Problems and Recommended Solutions," TR AGARDograph 16, Nov. 1957.

[14]Miller, D., Wright, W., Langhals, T., Al-Khalil, K., and Broughton, H., "Validation of NASA Thermal Ice Protection Computer Codes: Part 1—Program Overview," AIAA Paper 97-0049, Jan. 1997.

[15]Al-Khalil, K. M., Horvath, C., Miller, D. R., and Wright, W. B., "Validation of NASA Thermal Ice Protection Computer Codes: Part III—The Validation of ANTICE," AIAA Paper 97-0051, Jan. 1997.

[16]Brahimi, M. T., Tran, P., Chocron, D., Tezok, F., and Paraschivoiu, I., "Effect of Supercooled Large Droplets on Ice Accretion Characteristics," AIAA Paper 97-0306, Jan. 1997.

[17]Tran, P., Brahimi, M., and Paraschivoiu, I., "Ice Accretion on Aircraft Wings with Thermodynamic Effect," AIAA Paper 94-0605, Jan. 1994.

[18]Kays, W. M., and Crawford, M. E., *Convective Heat and Mass Transfer*, 3rd ed., McGraw–Hill, New York, 1993, Chaps. 10, 13, 20, and 21.

[19]Moran, J., *An Introduction to Theoretical and Computational Aerodynamics*, Wiley, New York, 1984, Chaps. 7 and 8.

[20]Meyer, C. A., *ASME Steam Tables*, 6th ed., American Society of Mechanical Engineers, New York, 1993, pp. 20–40.

[21]Press, W. H., Teukolsky, S. H., Vetterling, W. T., and Flannery, B., *Numerical Recipes in FORTRAN (The Art of Scientific Computing)*, 2nd ed., Cambridge Univ. Press, New York, 1992, Chap. 16.

[22]Tezok, F., and Fritz, E., "Icing Tunnel Testing Methodology," *Proceedings of the 6th Aerodynamics Symposium held in conjunction with Canadian Aeronautics and Space Institute 44th Annual Conference*, Ottawa, ON, Canada, April 1997, pp. 101–108.

[23]Batchelor, G. K., *An Introduction to Fluid Dynamics*, Cambridge Univ. Press, New York, 1967, pp. 219–221.